The Active Site of Methanol Synthesis over $Cu/ZnO/Al_2O_3$ Industrial Catalysts

Malte Behrens *et al.*

Science **336**, 893 (2012);
DOI: 10.1126/science.1219831

References and Notes

1. W. C. Conner, J. L. Falconer, *Chem. Rev.* **95**, 759 (1995).
2. V. V. Rozanov, O. V. Krylov, *Russ. Chem. Rev.* **66**, 107 (1997).
3. R. D. Cortright, R. R. Davda, J. A. Dumesic, *Nature* **418**, 964 (2002).
4. I. Ait-Ichou, M. Formenti, B. Pommier, S. J. Teichner, *J. Catal.* **91**, 293 (1985).
5. A. M. Hilmen, D. Schanke, A. Holmen, *Catal. Lett.* **38**, 143 (1996).
6. H. Cheng, L. Chen, A. C. Cooper, X. Sha, G. P. Pez, *Energy Environ. Sci.* **1**, 338 (2008).
7. K.-D. Jung, A. T. Bell, *J. Catal.* **193**, 207 (2000).
8. T. Ioannides, X. E. Verykios, *J. Catal.* **143**, 175 (1993).
9. R. B. Levy, M. Boudart, *J. Catal.* **32**, 304 (1974).
10. A. Higazy, M. Kassem, M. Sayed, *J. Phys. Chem. Solids* **53**, 549 (1992).
11. J. Kanellopoulos *et al.*, *J. Catal.* **255**, 68 (2008).
12. G. Ertl, *Angew. Chem. Int. Ed.* **47**, 3524 (2008).
13. S.-C. Li, L.-N. Chu, X.-Q. Gong, U. Diebold, *Science* **328**, 882 (2010).
14. S.-C. Li *et al.*, *J. Am. Chem. Soc.* **130**, 9080 (2008).
15. S. Wendt *et al.*, *Phys. Rev. Lett.* **96**, 066107 (2006).
16. H. C. Galloway, J. J. Benitez, M. Salmeron, *Surf. Sci.* **298**, 127 (1993).
17. J. L. Daschbach, Z. Dohnálek, S.-R. Liu, R. S. Smith, B. D. Kay, *J. Phys. Chem. B* **109**, 10362 (2005).
18. Y. Joseph, C. Kuhrs, W. Ranke, M. Ritter, W. Weiss, *Chem. Phys. Lett.* **314**, 195 (1999).
19. U. Leist, W. Ranke, K. Al-Shamery, *Phys. Chem. Chem. Phys.* **5**, 2435 (2003).
20. M. A. Henderson, *Surf. Sci. Rep.* **46**, 1 (2002).
21. W. X. Huang, W. Ranke, *Surf. Sci.* **600**, 793 (2006).
22. J. Knudsen *et al.*, *Surf. Sci.* **604**, 11 (2010).
23. See supplementary materials on *Science* Online.
24. G. Kresse, J. Furthmüller, *Phys. Rev. B* **54**, 11169 (1996).
25. J. P. Perdew, Y. Wang, *Phys. Rev. B* **45**, 13244 (1992).
26. P. E. Blöchl, *Phys. Rev. B* **50**, 17953 (1994).
27. G. Kresse, D. Joubert, *Phys. Rev. B* **59**, 1758 (1999).
28. H. Daiguji, *Nat. Nanotechnol.* **5**, 831 (2010).
29. G. M. Whitesides, *Nature* **442**, 368 (2006).

Acknowledgments: Supported by the Danish Research Agency, the Strategic Research Council, the Villum Kahn Rasmussen Foundation, the Carlsberg Foundation, the Lundbeck Foundation, Haldor Topsøe A/S, and the European Research Council through an advanced ERC grant. Work at the University of Wisconsin was supported by the U.S. Department of Energy, Basic Energy Sciences, Chemical Sciences Office. C.A.F. thanks NSF for a Graduate Research Fellowship. G.P., C.A.F., L.C.G., and M.M. thank the National Energy Research Scientific Computing Center, Pacific Northwest National Laboratory, Argonne National Laboratory, and Oak Ridge National Laboratory for computational resources and thank J. A. Dumesic for fruitful discussions.

Supplementary Materials

www.sciencemag.org/cgi/content/full/336/6083/889/DC1
Materials and Methods
Figs. S1 to S3
References (*30*–*40*)
Movies S1 to S4

23 January 2012; accepted 3 April 2012
10.1126/science.1219468

The Active Site of Methanol Synthesis over $Cu/ZnO/Al_2O_3$ Industrial Catalysts

Malte Behrens,[1]* Felix Studt,[2]* Igor Kasatkin,[1] Stefanie Kühl,[1] Michael Hävecker,[3] Frank Abild-Pedersen,[2] Stefan Zander,[1] Frank Girgsdies,[1] Patrick Kurr,[4] Benjamin-Louis Kniep,[4] Michael Tovar,[5] Richard W. Fischer,[4] Jens K. Nørskov,[2,6] Robert Schlögl[1]

One of the main stumbling blocks in developing rational design strategies for heterogeneous catalysis is that the complexity of the catalysts impairs efforts to characterize their active sites. We show how to identify the crucial atomic structure motif for the industrial $Cu/ZnO/Al_2O_3$ methanol synthesis catalyst by using a combination of experimental evidence from bulk, surface-sensitive, and imaging methods collected on real high-performance catalytic systems in combination with density functional theory calculations. The active site consists of Cu steps decorated with Zn atoms, all stabilized by a series of well-defined bulk defects and surface species that need to be present jointly for the system to work.

Methanol is produced industrially from synthesis gas mixtures ($H_2/CO_2/CO$) at elevated pressures P (50 to 100 bar) and temperatures T (200° to 300°C) over $Cu/ZnO/Al_2O_3$ catalysts, with a worldwide demand of ~50 Mtons $year^{-1}$. This catalytic system is also of interest for the potential use of methanol as a sustainable synthetic fuel obtained by hydrogenation of captured CO_2 (*1*). The phenomenological optimization of the preparation of catalytically very active "methanol copper" is far more advanced than the fundamental understanding of its high catalytic activity. The reaction mechanism of industrial methanol synthesis as well as the nature of the active site on Cu/ZnO-based high-performance catalysts have been debated (*2*) and are still not comprehensively understood. Here, we present experimental evidence for a structural model of the active site and use quantum chemical calculations to rationalize the experimentally observed structure-performance relation.

Industrial Cu/ZnO-based catalysts are prepared by a coprecipitation method (*3*) that creates porous aggregates of Cu and ZnO nanoparticles (NPs) (*4*) when Cu-rich molar compositions of Cu:Zn near 70:30 are used (*5*). The industrial system is a bulk catalyst characterized by a high Cu:Zn ratio with >50 mol% Cu (metal base), approximately spherical Cu NPs of a size around 10 nm, and ZnO NPs that are arranged in an alternating fashion to form porous aggregates. These aggregates expose a large Cu surface area of up to ~40 $m^2\ g^{-1}$. Furthermore, industrial catalysts contain low amounts of a refractory oxide as structural promoter (*6*), in most cases up to ~10% Al_2O_3. Omitting any of the constituting elements drastically reduces the performance of the system.

One important key to high performance is a large accessible Cu surface area (*7*), which has been observed to scale linearly with the activity for sample families with a similar preparation history (*8*). However, between these families considerably different intrinsic activities, that is, activities normalized by the Cu surface area, can be found. Thus, different "qualities" of Cu surfaces can be prepared that vary in the activity of their active sites and/or in the concentration of these sites. Hence, methanol synthesis over Cu appears to be a structure-sensitive reaction. Single-crystal studies (*9*–*11*) report turnover frequencies (TOF) for methanol synthesis ranging from as low as 1.3×10^{-6} to 6×10^{-3} s^{-1} per site.

ZnO functions as a physical spacer between Cu NPs and helps disperse the Cu phase in the course of catalyst preparation (*5*) and is thus responsible for the high Cu surface areas of industrial catalysts. However, the presence of ZnO increases the intrinsic activity of Cu-based methanol synthesis catalysts, an effect known as the Cu-ZnO synergy (*3*, *12*, *13*), and has led to many different (and conflicting) mechanistic models (*14*–*20*). This situation is partially the result of some models mainly having their bases in results from simplified samples, ranging from Cu single crystals to Cu NPs supported on highly crystalline ZnO with a low loading, that have compositions and microstructure that strongly deviate from that of the industrial catalyst described above.

Investigations on industrial samples and other coprecipitated systems have suggested that defects (*4*) and lattice strain (*21*) in the Cu NPs affect the intrinsic activity of the Cu surface. To study the role of defects in the real $Cu/ZnO/(Al_2O_3)$ composite system, we prepared a series of five functional catalysts and compared them to a pure Cu metal reference sample; details on the different samples can be found as

[1]Fritz-Haber-Institut der Max-Planck-Gesellschaft, Department of Inorganic Chemistry, Faradayweg 4-6, 14195 Berlin, Germany. [2]SUNCAT Center for Interface Science and Catalysis, SLAC National Accelerator Laboratory, 2575 Sand Hill Road, Menlo Park, CA 94025, USA. [3]Division Solar Energy Research, Elektronenspeicherring BESSY II, Helmholtz-Zentrum Berlin für Materialien und Energie, Albert-Einstein-Strasse 15, 12489 Berlin, Germany. [4]Süd-Chemie AG, Research and Development Catalysts, Waldheimer Straße 13, 83052 Bruckmühl, Germany. [5]Institute for Complex Magnetic Materials, Helmholtz-Zentrum Berlin für Materialien und Energie, Hahn-Meitner-Platz 1, 14109 Berlin, Germany. [6]Department of Chemical Engineering, Stanford University, Stanford, CA 94305, USA.

*To whom correspondence should be addressed. E-mail: behrens@fhi-berlin.mpg.de (M.B.); studt@slac.stanford.edu (F.S.)

supplementary information (tables S1 and S2) (*22*). All samples had a high Cu loading, Cu NPs sizes between 5 and 15 nm, and exposed Cu surface areas of 10 m^2 g^{-1} or greater. These properties made them similar to industrial catalysts. In order to allow for a reliable correlation of catalytic and structural data, the microstructural homogeneity of the prepared catalysts was carefully checked. Samples were prepared from nearly single-phase precursor materials, which resulted in relatively homogeneous element distributions and monomodal Cu NP size distributions after thermal treatment (figs. S1 to S3) (*22*). The catalytic activity of all six samples (Fig. 1A) was measured under industrial conditions at $P = 60$ bar and $T = 210°$ and 250°C in a typical syngas mixture (*22*). The ZnO-free Cu reference exhibited little activity, whereas the catalysts that performed best were prepared following the industrial synthesis method. Dividing the performance by the Cu surface areas results in the intrinsic activities, which are shown in Fig. 1B normalized to the intrinsically most active catalyst for each temperature. The scatter of the data shows that the Cu surface area alone cannot explain the differences in performance. The use of the full exposed Cu surface area for a formal calculation of TOFs resulted in values varying from 5.4×10^{-4} for the pure Cu reference to 2.1×10^{-2} s^{-1} per site for the intrinsically most active samples; this value is at the medium to higher end of the reported values (*9*–*11*).

To find a structural explanation for the observed trend, we performed neutron diffraction experiments on the reduced catalysts. Broad peaks of the metallic Cu face-centered cubic (fcc) phase indicative of small crystallite domains (3.8 to 9.9 nm) were present in all catalyst samples (tables S3 and S4 and fig. S4) (*22*). The inactive pure Cu reference sample exhibited sharper peaks and larger domains of >100 nm. We performed an analysis of the planar defect structure by using a pattern decomposition method (table S5) (*22*). Characteristic diffraction peaks will broaden and shift from their ideal position as a function of increased stacking fault concentration (*23*). The shift of the 111 and 200 peaks toward each other and the simultaneous shift of the higher-order peaks 222 and 400 away from each other are especially characteristic of stacking faults. The neutron scattering data allowed for a sufficiently reliable fitting of the 400 peak position of the nanostructured Cu phase. The ratios $d_{hhh}/d_{(2h)00}$ for $h = 1$, 2, which are expected to be constant at $2/\sqrt{3} = 1.1547$ for an ideal fcc structure, are shown in Fig. 1C. For the inactive pure Cu sample, both ratios fall near the expected ideal value, whereas the catalytically active materials showed a lower value for $h = 1$ and a higher one for $h = 2$, which is consistent with the presence of stacking faults in the Cu particles. For quantification (Fig. 1C), we used the spacing of the more intensive 111 and 200 peaks (*24*); the resulting stacking fault density (Fig. 1D) scales linearly with the intrinsic activity. The highly active methanol copper is a defective form of nanoparticulate Cu rich in planar defects like stacking faults. The high abundance of defects in the active materials is tentatively related to the confined crystallization of the Cu NPs in strong interfacial contact with the ZnO component during the mild catalyst activation procedure, leading to a kinetically trapped form of Cu.

The nonideal nature of active Cu is also manifested as microstrain, to which lattice defects will contribute. The absolute amount of strain, although not negligible, is not large enough to cause substantial changes in the binding energies or barriers. Typically, defects appear as a mechanism of strain relaxation, and some residual strain is concentrated around them. Thus, defects can be considered as being coupled to strain (*22*). Accordingly, we found in our series of samples a coarse trend of the intrinsic activity with higher lattice strain (fig. S5) (*22*). The general importance of strain for Cu/ZnO catalysts has been highlighted before (*4*, *21*). We suggest that the main role of the bulk defects for catalysis is that an extended defect induces a line defect at the exposed surfaces—typically a step, as can be observed in Fig. 1D, which shows how a stacking

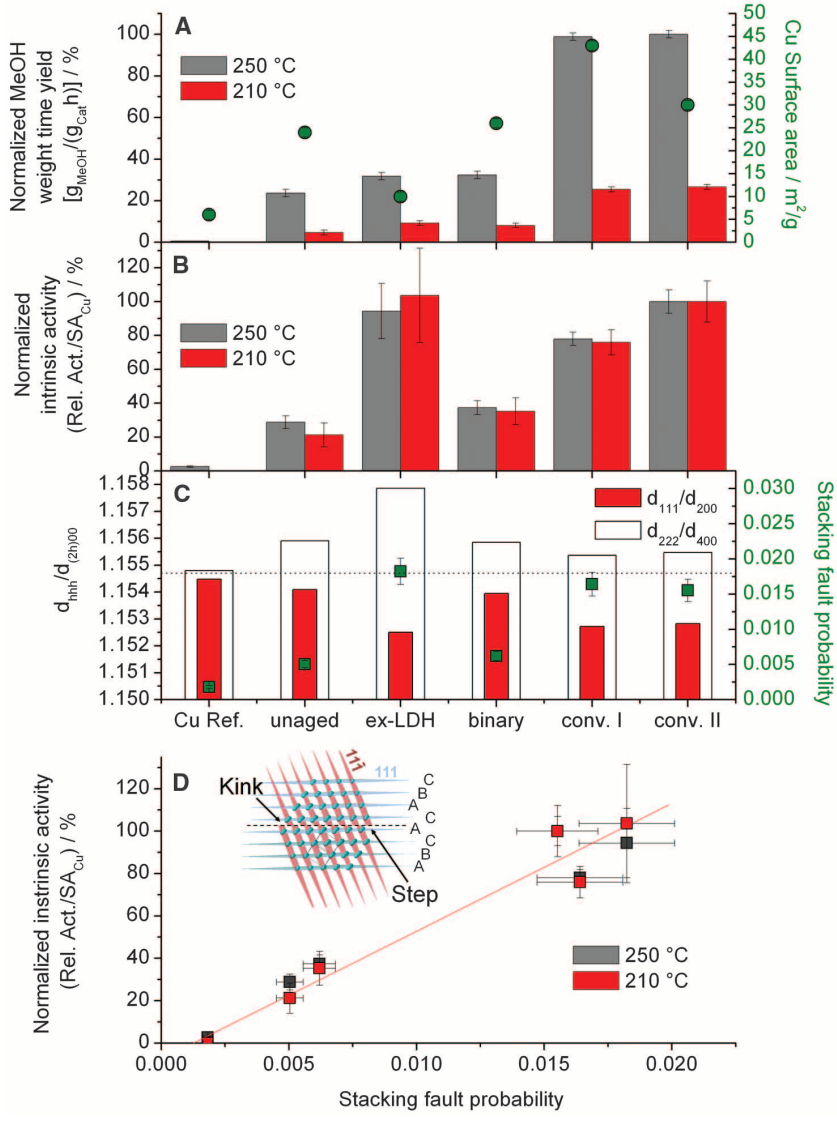

Fig. 1. (**A**) Catalytic activities and Cu surface areas of the Cu reference material and the five Cu/ZnO/Al_2O_3 catalysts in methanol synthesis (P = 60 bar, T = 210°, 250°C, normalized to the most active sample). (**B**) Intrinsic activities per Cu surface area obtained after dividing by the Cu surface area (normalized: most active sample = 100% at each temperature). (**C**) Deviation of d_{111}/d_{200} and d_{222}/d_{400} observed in the neutron diffraction patterns and resulting stacking fault probabilities of the Cu particles. The dashed line refers to the ideal fcc structure. For a detailed description of the samples and explanation of sample labeling, see (*22*). (**D**) Relation of the intrinsic activity of Cu to the concentration of stacking faults. (Inset) Schematic of how a stacking fault in 111 can generate kinks and surface steps in the $11\bar{1}$ facet. Error bars indicate uncertainties determined on basis of replicate measurements (catalytic activity and copper surface area). The error bar of the diffraction peak analysis is based on an estimated uncertainty of 0.1% for the angular peak position.

fault in 111 creates a step on the $11\bar{1}$ surface of a Cu crystallite. A twin boundary terminating at a surface is associated with a kink.

The effect of steps at the Cu surface on the catalytic properties was also confirmed by density functional theory (DFT) calculations on different Cu surfaces. In this study, DFT was used to provide qualitative confirmation of the experimentally observed trends and to rationalize the effect of the structural features that have been identified to be relevant for the catalytic properties of the catalyst's surface. To attain some independence of presumptions on the reaction mechanism, we studied methanol formation from both CO_2 and CO (*25*). A flat Cu(111) surface represents the ideal defect-free catalyst, whereas a stepped Cu(211) surface was used to include the effect of surface defects (Fig. 2, black and blue curves). Figure 2B shows the CO_2 hydrogenation pathway on the two different surfaces. For clarity, only the lowest-energy pathway is shown, which is the same for both surfaces. Energetics of the other intermediates are given in tables S6 to S8 (*22*). The barrier for the splitting of molecular hydrogen was calculated to be 0.74 and 0.84 eV on the Cu(211) and Cu(111) surfaces, respectively, so surface hydrogen was readily available under reaction conditions. Hydrogenation of CO_2 proceeded via formation of HCOO, HCOOH, and H_2COOH. The C-O bond of H_2COOH was split to yield adsorbed H_2CO and OH, where H_2CO is hydrogenated to methanol via the methoxy (CH_3O) intermediate. Surface OH was removed as water. A similar pathway for CO_2 hydrogenation on the (111) surface of Cu has been suggested recently (*26*). Other theoretical studies of this reaction have considered Cu(100) (*27*), small Cu clusters (*28*), or Zn atoms deposited on Cu(111) (*29*).

As shown in Fig. 2B, the flat Cu(111) surface bound the intermediates more weakly than did Cu(211). Essentially all intermediates are thermodynamically less stable than CO_2 and H_2 in the gas phase. Note that these thermodynamics include effects of pressure; high CO_2 and H_2 pressure strengthen adsorption energies and make the formation of methanol and water downhill in energy, explaining why high pressures are needed for this process. Both the energies of the intermediates and the transition-state were stabilized considerably for the (211) surface compared with the (111) surface, rendering the steps more active than the terraces. Similar results were obtained for hydrogenation of CO to methanol (Fig. 2C). CO hydrogenation proceeded via hydrogenation of the carbon atom of CO, with the intermediates being HCO, H_2CO, and H_3CO. H_3CO was then hydrogenated to methanol. The last two intermediates are the same as for the hydrogenation of CO_2. Steps again lower the adsorption energies of the intermediates substantially compared with the flat surface.

The stepped Cu(211) surface or the stacking fault-created step shown in the inset of Fig. 1D can be regarded as model situations. We also examined the relation of bulk defects and surface steps in the most active catalyst with aberration-corrected high-resolution transition electron microscopy (HRTEM). The vast majority of the investigated Cu NPs were faulted and exhibited planar extended defects, stacking faults, and twin boundaries that ran through the whole particle. It can be seen from the micrographs in Fig. 3 that the NP shapes can be generally approximated by a sphere. The curvature of the particle causes the surface to intrinsically contain a number of steps. The HRTEM image in Fig. 3A shows stepped surface facets like (211) and (522) being responsible for the curvature at the lower exposed side of the Cu NP. Surface faceting also changed along the line where the twin boundary terminates at the surface. This kind of kink is associated with an inward curvature of the surface, which does not occur on regular spherical or ellipsoidal fcc particles or Wulff polyhedra. Another example (Fig. 3B) showed a pattern of planar bulk defects (twin boundaries), as reflected in changes of the surface faceting creating a local inward curvature of the NP. Despite the absence of stepped surface facets at this part of the NP, a number of steps were created by the inward kinks, where the twin boundaries meet the surface. Figure 3C shows that twin boundaries could create distinctive surface ensembles even if the Cu surface of a larger NP appears essentially flat. The change of the surface faceting

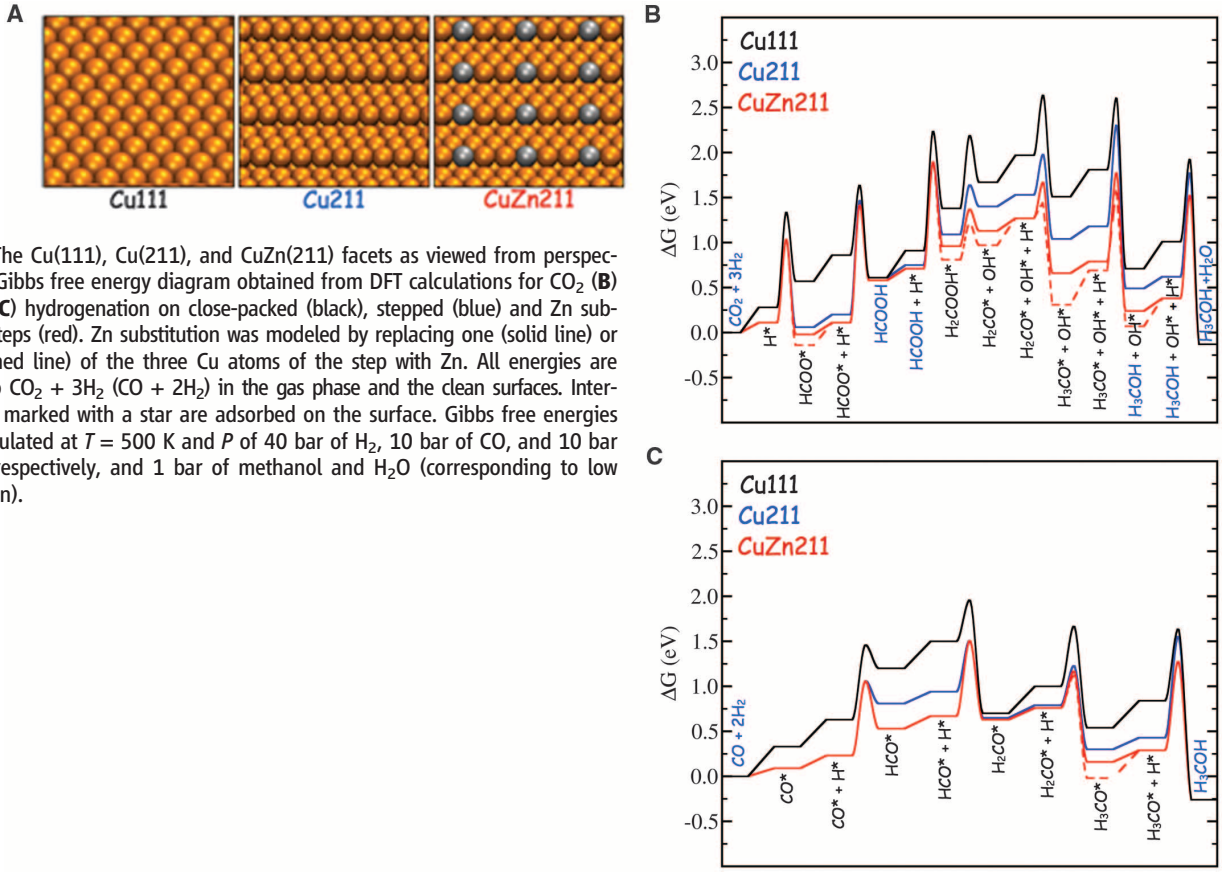

Fig. 2. The Cu(111), Cu(211), and CuZn(211) facets as viewed from perspective (**A**). Gibbs free energy diagram obtained from DFT calculations for CO_2 (**B**) and CO (**C**) hydrogenation on close-packed (black), stepped (blue) and Zn substituted steps (red). Zn substitution was modeled by replacing one (solid line) or two (dashed line) of the three Cu atoms of the step with Zn. All energies are relative to $CO_2 + 3H_2$ ($CO + 2H_2$) in the gas phase and the clean surfaces. Intermediates marked with a star are adsorbed on the surface. Gibbs free energies were calculated at $T = 500$ K and P of 40 bar of H_2, 10 bar of CO, and 10 bar of CO_2, respectively, and 1 bar of methanol and H_2O (corresponding to low conversion).

from (111) to (100) is associated only with a slightly obtuse angle near 180°. Neighboring to the position of the kink, a column of surface atoms was observed whose position stuck out of the regular surface (Fig. 3D, arrow). Again, such an arrangement can be described as a high-energy site created by the termination of a planar defect at the surface of the Cu NP.

Because the presence of a defect at the active site alone does not directly involve ZnO, it cannot explain the observation (*12*, *13*) of Cu-ZnO synergy in physical mixtures. It seems likely that the Cu-ZnO synergy is related to strong metal support interaction (SMSI) between Cu and ZnO leading to a partial coverage of the Cu surface with ZnO_x under reducing conditions. SMSI has been observed on Cu/ZnO-based catalysts by using vibrational spectroscopy (*30*) and thermal desorption of probe molecules (*31*) and by monitoring the wetting behavior of Cu/ZnO model catalysts (*32*). In the high-performance catalyst studied here, the presence of a disordered overlayer of the Cu NPs with a thickness of about 1 nm can be seen in some HRTEM images (Fig. 3, B and C). In the complex real catalyst, fully covered NPs coexist with partially covered and practically uncovered ones. To identify the layer as ZnO_x, we investigated the surface composition of the most active catalyst by using ambient pressure x-ray photoemission spectroscopy (XPS). In agreement with previously reported data (*16*, *33*), the Cu:Zn ratio at the catalyst's surface dropped during activation in hydrogen. For our catalyst, the Cu:Zn ratio was inverted from its nominal value of 70:30 (calcined) to ~30:70 (reduced), supporting the idea of an SMSI effect (Fig. 4A). The (partial) ZnO_x coverage of the surface of the reduced Cu NPs in the catalyst was also evidenced by tuning the information depth of the experiment from about 0.6 to 2.3 nm by variation of the kinetic energy of the incoming x-ray beam (Fig. 4B). Core level fitting of the Zn 3p and Cu 3p signals showed the enrichment of Zn at the surface of the catalyst (fig. S6) (*22*), whereas with a higher information depth the Cu:Zn ratio is slowly approaching toward the nominal composition. The calcined catalyst did not show any surface enrichment of Zn, and the effect was fully reversible upon recalcination of the catalyst. Given the dynamics of the ZnO component in this Cu/ZnO catalyst and the observation of surface decoration of the Cu NPs already at relatively mild conditions of low partial pressure of hydrogen, further progression of this effect under strongly reducing conditions may lead to formation of a CuZn surface alloy, as discussed by several authors (*3*, *30*, *32*).

The beneficial role of Zn at the catalyst's surface can be explained by DFT calculations. To incorporate the effect of Zn, we studied a Cu(211) surface where Cu in the step is partially substituted by Zn (Fig. 2, red curves). Alloying of Zn into the Cu step further increased the adsorption strength of HCO, H_2CO, and H_3CO and decreased the barriers. Hence, the rate of methanol synthesis was further increased. The order of activity for CO_2 as well as for CO hydrogenation is CuZn(211) > Cu(211) > Cu(111). The most active surface was therefore found to be a Cu step with Zn alloyed into it. The adsorption properties of alloyed CuZn(111) surface have been experimentally observed to be modified from those of pure Cu(111) (*18*). Indeed, species that are bound to the surface through oxygen atoms, such as formate and hydroxyl,

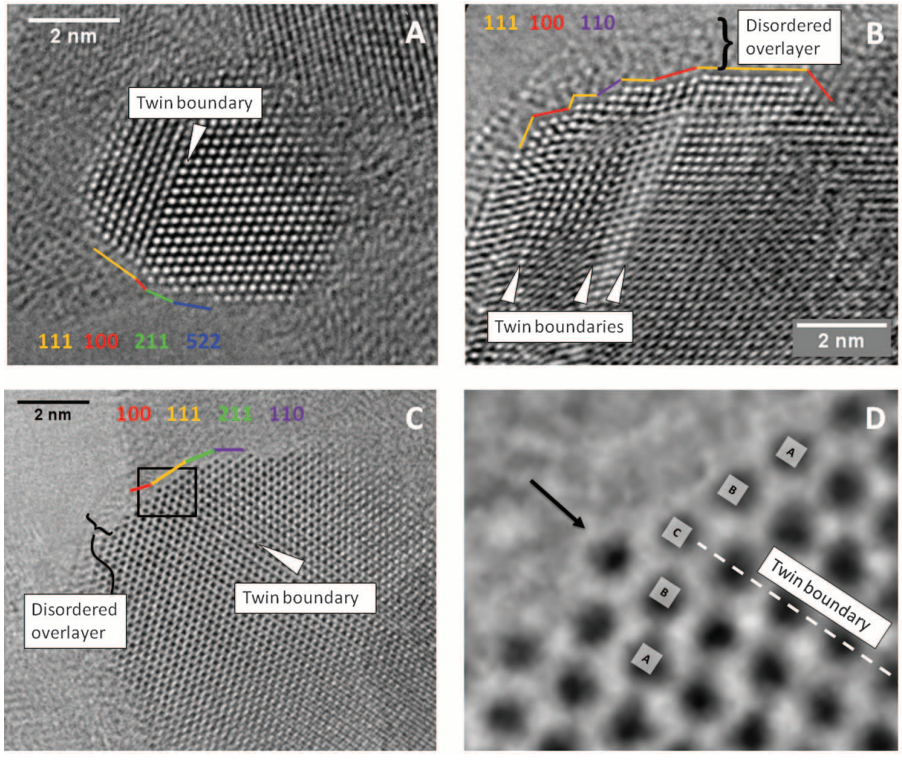

Fig. 3. (**A** to **D**) Aberration-corrected HRTEM images of Cu particles in the conventionally prepared, most-active $Cu/ZnO/Al_2O_3$ catalyst. (D) is a close-up of the marked area in (C).

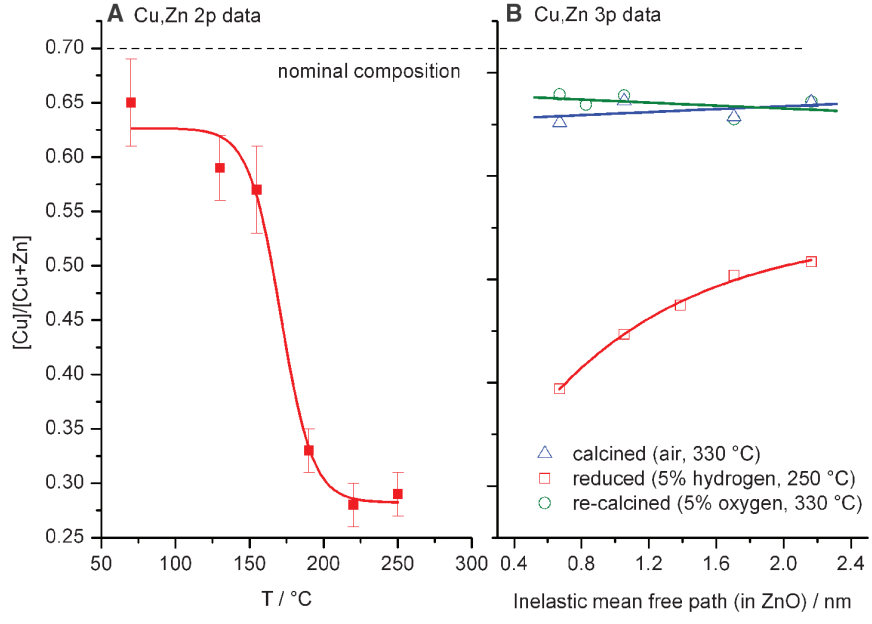

Fig. 4. Surface and near-surface composition of the most active $Cu/ZnO/Al_2O_3$ catalyst of this study with a Cu:Zn ratio of 70:30 recorded with synchrotron XPS. (**A**) In situ Cu, Zn 2p data during reduction in 0.25 mbar hydrogen with a heating rate of 2 K min^{-1}. Error bars represent estimated uncertainty based on several fits with random variation of background fitting parameters. (**B**) Environmental Cu, Zn 3p data of the calcined, the pre-reduced (in 5% hydrogen at 250°C) and recalcined (5% oxygen at 330°C) catalyst as a function of information depth. Lines are guides to the eye.

will widely cover the surface of the catalyst under methanol synthesis conditions. If more Zn atoms are considered in the CuZn(211) surface, the binding to these species is further strengthened (Fig. 2). According to this trend and in agreement with the higher oxophilicity of Zn compared with Cu, these species will bind to the surface via Zn atoms, leading to a formal oxidation of the Zn component. Thus, under steady-state conditions, the oxidation state of Zn is adjusted to a partially oxidized $Zn^{\delta+}$ state, which can be formed by reduction from the ZnO particles through SMSI as well as from a CuZn surface alloy by adsorbate-induced oxidation. The unique role of ZnO in the industrial catalyst is probably related to the stability of this intermediate oxidation state under the reducing potential of methanol synthesis conditions. Its reducibility is high enough to allow for partial reduction but sufficiently low not to favor bulk alloying. Other promoters that bind oxygen in the same range as Zn may have a similar effect. The Cu/ZrO_2 system, for example, is also an active methanol synthesis catalyst (*34*).

Combining the experimental and theoretical results, a model for the active site of methanol synthesis over industrial catalysts emerges. Undistorted pure Cu was quite inactive in the methanol synthesis experiment. The same result was obtained for the flat Cu(111) surface in the DFT calculations. High activity was generated by two factors. First, the presence of steps at the Cu surface is required, which can be stabilized by bulk defects like stacking faults or twin boundaries terminating at the surface. The increase in activity is explained by a stronger binding of the intermediates on stepped sites and lower energy barriers between them. The bulk defect structure in the real catalyst is a result of a well-optimized low-temperature preparation method.

The second requirement is the presence of $Zn^{\delta+}$ at the defective (stepped) Cu surface, which in the high-performance catalyst is a result of a dynamic SMSI effect leading to partial coverage of the metal particles with ZnO_x. Substitution of Zn into the Cu steps further strengthens the binding of the intermediates and increases the activity of the catalyst. The data presented suggest that the presence of steps and their close proximity to ZnO_x on the surface of the Cu particles create the ensemble needed to render the very active methanol copper: a Cu step with a nearby Zn serving as adsorption site for oxygen-bound intermediates.

These two requirements are fulfilled only for a small and varying fraction of the metallic Cu surface area, explaining the differences in intrinsic activity observed here and also in literature. Thus, under industrially relevant conditions a small fraction of the surface is largely contributing to the activity, which cannot be easily mimicked by simplified model approaches. We propose that the TOF of this reaction channel should be considerably higher compared with the values calculated on the basis of the full exposed Cu surface area.

References and Notes

1. G. A. Olah, A. Goeppert, G. K. Surya Prakash, *Beyond Oil and Gas: The Methanol Economy* (Wiley-VCH, Weinheim, Germany, 2006).
2. J. B. Hansen, P. E. Højlund Nielsen, in *Handbook of Heterogenous Catalysis*, G. Ertl, H. Knözinger, F. Schüth, J. Weitkamp, Eds. (Wiley-VCH, Weinheim, Germany, ed. 2, 2008), pp. 2920–2949.
3. M. S. Spencer, *Top. Catal.* **8**, 259 (1999).
4. I. Kasatkin, P. Kurr, B. Kniep, A. Trunschke, R. Schlögl, *Angew. Chem.* **119**, 7465 (2007).
5. M. Behrens, *J. Catal.* **267**, 24 (2009).
6. M. Kurtz, H. Wilmer, T. Genger, O. Hinrichsen, M. Muhler, *Catal. Lett.* **86**, 77 (2003).
7. The exposed Cu surface area can be measured using reactive chemisorption of N_2O, which leads to a surface oxidation of Cu ideally yielding a Cu_2O monolayer.
8. M. Kurtz *et al.*, *Catal. Lett.* **92**, 49 (2004).
9. J. Yoshihara, C. T. Campbell, *J. Catal.* **161**, 776 (1996).
10. P. B. Rasmussen *et al.*, *Catal. Lett.* **26**, 373 (1994).
11. J. Szanyi, D. W. Goodman, *Catal. Lett.* **10**, 383 (1991).
12. R. Burch, S. E. Golunski, M. S. Spencer, *J. Chem. Soc. Faraday Trans.* **86**, 2683 (1990).
13. Y. Kanai, T. Watanabe, T. Fujitani, T. Uchijima, J. Nakamura, *Catal. Today* **28**, 223 (1996).
14. K. Klier, *Adv. Catal.* **31**, 243 (1982).
15. V. Ponec, *Surf. Sci.* **272**, 111 (1992).
16. W. P. A. Jansen *et al.*, *J. Catal.* **210**, 229 (2002).
17. J. C. Frost, *Nature* **334**, 577 (1988).
18. J. Nakamura, Y. Choi, T. Fujitani, *Top. Catal.* **22**, 277 (2003).
19. K. C. Waugh, *Catal. Today* **15**, 51 (1992).
20. P. L. Hansen *et al.*, *Science* **295**, 2053 (2002).
21. M. M. Günter *et al.*, *Catal. Lett.* **71**, 37 (2001).
22. See supplementary materials on *Science* Online.
23. This effect arises from the generation of thin hexagonal domains in the cubic lattice with the change in stacking sequence of the hexagonally close-packed (111) layers at the stacking fault (ideal is A-B-C-A; stacking fault, A-B-C-B-C-A; twin boundaries, A-B-C-B-A). For more details and quantitative treatment see, e.g., (*24*).
24. B. E. Warren, *X-ray Diffraction* (Dover, New York, 1990).
25. G. C. Chinchen, P. J. Denny, J. R. Jennings, M. S. Spencer, K. C. Waugh, *Appl. Catal.* **36**, 1 (1988).
26. L. C. Grabow, M. Mavrikakis, *ACS Catal.* **1**, 365 (2011).
27. Z.-M. Hu, K. Takahashi, H. Nakatsuji, *Surf. Sci.* **442**, 90 (1999).
28. Y. Yang, J. Evans, J. A. Rodriguez, M. G. White, P. Liu, *Phys. Chem. Chem. Phys.* **12**, 9909 (2010).
29. Y. Morikawa, K. Iwata, K. Terakura, *Appl. Surf. Sci.* **169–170**, 11 (2001).
30. N.-Y. Topsøe, H. Topsøe, *Top. Catal.* **8**, 267 (1999).
31. R. Naumann d'Alnoncourt *et al.*, *Phys. Chem. Chem. Phys.* **8**, 1525 (2006).
32. J. D. Grunwaldt, A. M. Molenbroek, N. Y. Topsoe, H. Topsoe, B. S. Clausen, *J. Catal.* **194**, 452 (2000).
33. J. Słoczynski *et al.*, *Appl. Catal. A Gen.* **310**, 127 (2006).
34. I. A. Fisher, H. C. Woo, A. T. Bell, *Catal. Lett.* **44**, 11 (1997).

Acknowledgments: We thank M. Muhler and O. Hinrichsen for fruitful discussions. M.B., I.K., S.K., S.Z. F.G., and R.S. acknowledge the Bundesministerium für Bildung und Forschung (FKZ 01RI0529) and Süd-Chemie AG for financial support. P.K., B.-L.K., and R.W.F. thank the Bayerisches Wissenschaftsministerium (NW-0810-0002) for financial support of this work. F.S., F.A.-P., and J.K.N. wish to acknowledge support from the (U.S.) Department of Energy, Office of Basic Energy Sciences. The data presented in this work can be obtained from the corresponding authors upon request.

Supplementary Materials

www.sciencemag.org/cgi/content/full/science.1219831/DC1
Materials and Methods
Supplementary Text
Figs. S1 to S6
Tables S1 to S8
References (*35–52*)

30 January 2012; accepted 3 April 2012
Published online 19 April 2012;
10.1126/science.1219831

Structures of Cage, Prism, and Book Isomers of Water Hexamer from Broadband Rotational Spectroscopy

Cristóbal Pérez,[1] Matt T. Muckle,[1] Daniel P. Zaleski,[1] Nathan A. Seifert,[1] Berhane Temelso,[2] George C. Shields,[2]* Zbigniew Kisiel,[3]* Brooks H. Pate[1]*

Theory predicts the water hexamer to be the smallest water cluster with a three-dimensional hydrogen-bonding network as its minimum energy structure. There are several possible low-energy isomers, and calculations with different methods and basis sets assign them different relative stabilities. Previous experimental work has provided evidence for the cage, book, and cyclic isomers, but no experiment has identified multiple coexisting structures. Here, we report that broadband rotational spectroscopy in a pulsed supersonic expansion unambiguously identifies all three isomers; we determined their oxygen framework structures by means of oxygen-18–substituted water ($H_2{}^{18}O$). Relative isomer populations at different expansion conditions establish that the cage isomer is the minimum energy structure. Rotational spectra consistent with predicted heptamer and nonamer structures have also been identified.

The intermolecular hydrogen-bonding interactions of water are responsible for many remarkable physical properties of the liquid and solid phases of the compound and furthermore play a pivotal role in solution chemistry and biochemistry. As a result, the accurate description of the water intermolecular potential is one of the most important problems in chemistry (*1*). One key method for quantitative analysis of water interactions is the size-selective study of the structures of water clusters (*2–5*). This problem has been attacked using several state-of-the-art techniques, including far-infrared (FIR) spectroscopy (*6–9*), helium nanodroplet isolation (HENDI) spectroscopy (*10*), infrared spectroscopy of size-selected molecular beams (*11*), molecular tagging ion-dip infrared spectroscopy (*12*, *13*), and argon-mediated, population-modulated attachment spectroscopy (*14*). Here, we report chirped-pulse Fourier transform microwave